Chapter 20

SOFT LASER DESORPTION IONIZATION - MALDI, DIOS AND NANOSTRUCTURES

Akos Vertes
Department of Chemistry, Institute for Proteomics Technology and Applications, The George Washington University, Washington DC 20052

1. INTRODUCTION

In 1948, Arne Tiselius won the Nobel Prize in chemistry for the discovery of electrophoresis and its application to analyze large molecules, specifically complex serum proteins. During the following decades, gel electrophoresis and its derivative techniques became a central method for molecular biology. They allowed for the identification of molecular mass with an accuracy of ~1 kDa, i.e., a thousand atomic mass units. Although this method enabled the separation of thousands of proteins from biological samples, the determination of the actual molecular weight, and with it finding the true identity of many substances, remained unachievable.

When it came to accurate mass determination of small molecules, mass spectrometry was the method of choice. However, for the accurate mass analysis of large molecules, their low volatility presented a fundamental obstacle. Typically, the larger the molecule, the harder it is to transfer it into the gas phase without degradation. Depositing the energy necessary for volatilization initiates other competing processes that elevate the internal energy of the adsorbate and results in its fragmentation. This competition between evaporation (or desorption) and fragmentation was recognized early on and the method of rapid heating was proposed to minimize the latter (Beuhler, et al., 1974). Lasers with submicrosecond pulse length were appealing tools for rapid heating but the initial results indicated limitations with respect to the ultimate size of the biomolecules ($m/z < 1{,}500$) that could be successfully analyzed (Posthumus ,et al., 1978). The goal of probing large molecules with laser desorption mass spectrometry remained elusive for a decade.

After a frustrating period of near misses in the early 1980's, in 1988 the quest to desorb and ionize large peptides and proteins using pulsed laser radiation succeeded (Tanaka, et al., 1988; Karas and Hillenkamp, 1988). As a result, during the past decade soft laser desorption ionization (SLDI) methods have become indispensable in the mass spectrometric analysis of biomolecules. With the analytical needs in the biomedical field—most notably in genomics, proteomics and metabolomics—multiplying, there is a continuous impetus to enhance the existing methods and explore new ones.

The first, and thus far most successful, SLDI technique is matrix-assisted laser desorption ionization (MALDI). In this method, the sample is mixed with an organic matrix that efficiently absorbs the laser energy. Upon exposure to pulsed laser radiation, the ensuing phase transition of the matrix volatilizes the large molecules. A small fraction of these molecules are also ionized enabling the mass spectrometric determination of their accurate mass. The combination of MALDI with mass spectrometry (MALDI-MS) is an enabling technology for the emerging discipline of proteomics. For the discovery of SLDI, in 2002 Koichi Tanaka became a corecipient of the Nobel Prize in chemistry.

The improvement in the accuracy of molecular mass determination brought about by MALDI was monumental. While for 10 kDa proteins the mass accuracy of gel electrophoresis was at best ~1%, MALDI routinely provided ~10 ppm. This thousand-fold improvement enabled the identification of post-translational modifications, a feature responsible for determining the biological function of proteins.

The utility of MALDI-MS for the analysis of large molecules inspired related efforts to use SLDI for the investigation of low molecular mass compounds. Due to the overwhelming matrix signal, MALDI itself had limited capabilities in the low mass region. In 1999, based on a nanoporous silicon substrate Siuzdak and coworkers introduced an efficient SLDI method termed desorption ionization on silicon (DIOS) (Wei, et al., 1999).

It was assumed that the substrate used in this technique derived its utility from the nanoporous structure. This hypothetical link between nanostructured surfaces and their enhanced desorption ionization properties initiated a host of laser desorption studies on nanomaterials. The considered systems included quasi-one-dimensional structures, such as nanopores (Wei, et al., 1999), nanotubes (Xu, et al., 2003), nanowires (Go, et al., 2005) and nanogrooves (Okuno, et al., 2005), nanoparticles (McLean, et al., 2005) and their aggregate phases, e.g., nanoparticle films, (Chen, et al., 2005; Luo, et al., 2005b) and, more recently, ordered arrays of silicon nanocavities (Finkel, et al., 2005) and microcolumns (Chen and Vertes, 2005; Chen, et al., 2005). Ion production from all of these surfaces was demonstrated for small to midsize molecules, including peptides, up to ~6 kDa.

There are four processes that determine the abundance and properties of the generated ions in SLDI: energy deposition, phase change, ionization and energy redistribution. As all the events are driven by the energy of the laser pulse, energy deposition, i.e., coupling of the laser energy into the target is an important factor. The efficiencies of phase change and ionization control the ion yields, whereas the increase in the internal energy of the produced ions due to energy redistribution promotes their fragmentation. The objective of this chapter is to explore the contribution of these processes to MALDI and to the other emerging SLDI methods. While there is a growing body of knowledge on the mechanistic aspects of MALDI, the nature and role of the decisive factors in SLDI from nanostructures is in a nascent state. Beyond the straightforward surface area effects, the potential role of phenomena specific to nanomaterials, such as quantum confinement and nanoscopic liquid confinement, as well as near-field effects, is considered.

2. MATRIX-ASSISTED LASER DESORPTION IONIZATION

2.1 Energy deposition – nonlinear effects

It was clear early on that matching the laser pulse parameters (wavelength and fluence, and to a certain degree pulse duration) with the optical and thermal properties of the matrix was critically important to the success of the MALDI experiment. Matrix materials were selected, in part, based on their linear optical properties at the wavelength of the laser radiation. Solid phase optical absorption coefficients of the most successful matrix materials in the near-ultraviolet (UV) are in the 10^4 to 10^5 cm^{-1} range (Allwood, et al., 1996, 1997). For example, the linear (low fluence) absorption coefficient of 2,5-dihydroxybenzoic acid (2,5-DHB) at the nitrogen laser wavelength of 337 nm is $\alpha = 7.95\times10^4$ cm^{-1}. Similarly, water ice is a MALDI matrix in the infrared (IR) at ~2.94 μm, where the OH vibration band gives rise to efficient linear absorption, $\alpha = 1.2\times10^4$ cm^{-1}.

Nonlinear absorption effects are generally considered negligible in MALDI (Dreisewerd, 2003). While this might be true for UV excitation at the ion generation threshold, at other wavelengths and/or higher laser fluences nonlinear absorption can be expected. In practice, experiments are not always carried out at the threshold fluence. A possible cause of nonlinearity is the high linear absorption coefficient of the matrix, as it helps to populate the excited states. Thus, if the excited state lifetime is sufficiently long the matrix material can behave as a saturable absorber and with increasing fluence become more and more transparent.

The nonlinear optical properties of the UV matrix materials are not known. There is data, however, for matrixes in the mid-IR that supports the hypothesis that nonlinear absorption plays a role. Careful optical absorption measurements as a function of laser fluence indicate that at 2.94 μm wavelength the absorption coefficient of water declines as the energy density of the material increases (Shori, et al., 2001). This effect can be explained by the disruption of the hydrogen bond network due to heating by the laser pulse (Bencsura and Vertes, 1995). This weakening of the non-covalent water structure gives rise to a blue shift of the absorption resonance and, thus, to reduced absorption at 2.94 μm. For example, the transmission of a 4.26 μm water layer increases from ~0.5% in the low fluence limit (linear absorption) to 11% at 0.8 J/cm^2 laser fluence, a value only slightly higher than the fluence threshold for IR-MALDI (see Fig. 2 in Shori, et al., 2001).

A similar blue shift was observed in IR-MALDI experiments. For certain matrixes (phloroglucin, triethanolamine, and glycerol), the ionization threshold fluence as a function of wavelength in the 2.7–3.6 μm range showed a minimum that was blue shifted compared to the absorption maximum of the low intensity (linear) optical absorbance (Menzel et al., 2001). In the same study, the nonlinear behavior for glycerol was confirmed through fluence dependent optical absorption measurements.

There are two major consequences of the nonlinear optical response regarding energy deposition. First, the laser light penetrates deeper into the target than what one would expect from the linear theory. Second, the temperature distribution in the target exhibits a maximum at a finite depth beneath the surface. As it is shown in section 2.2, these two factors have important implications for material removal and plume dynamics.

Sample morphology also plays a special role in the efficiency of energy deposition. It is known that upon repeated laser exposure of a polycrystalline MALDI target, the smaller crystallites and/or the thinner crystal features evaporate first. This preferential ablation dramatically accelerates when the thermal diffusion length and the smallest dimension of a crystallite are comparable in size (Sadeghi and Vertes, 1998). In these systems, energy dissipation through heat conduction is limited. This leads to rapidly escalating temperatures, superheating and eventually phase explosion in the entire crystallite. Sample morphology (texture) was also found to influence the laser fluence threshold necessary to produce matrix ions. Studying pressed pellet samples, it was shown that with increasing the pressure used to produce the pellet structural coarsening occurred and, as a result, the threshold fluence increased (Chen and Vertes, 2003). While these morphology effects are significant in MALDI, they are expected to be even more important, perhaps even dominant, in SLDI from nanostructured surfaces.

Current models of MALDI do not incorporate nonlinear absorption and morphology effects. For a broad class of conditions, realistic estimates of target heating cannot be given without accounting for these aspects of energy deposition.

2.2 Surface evaporation vs. phase explosion

In MALDI, the molecules of interest are embedded into the matrix crystals. Volatilization of the analyte relies on a phase transition induced by fast laser heating. Due to the extreme heating rates produced by the short laser pulse ($>10^6$K/s), the surface layers of the matrix become superheated. Once the spinodal decomposition temperature is reached, these layers undergo phase explosion. Before and after the phase explosion, vigorous surface evaporation takes place. The relative importance of phase explosion and surface evaporation depends on laser fluence, pulse length, and matrix material parameters.

Experimental evidence for the presence of both of these processes was found in ion and neutral velocity measurements in vacuum (e.g., Juhasz, et al., 1997), and for atmospheric pressure MALDI (AP-MALDI) conditions, in shock front velocity measurements (Apitz and Vogel, 2005). The velocities in vacuum are typically in the few hundred m/s range with variations detected for different matrixes and analytes.

To follow the plume dynamics stemming from surface evaporation in vacuum, a fluid dynamics model was used (Vertes, et al., 1993). The model enabled the description of density, velocity and temperature distributions in and above the target for a period of 100 ns. It gave good predictions for neutral velocities and for the desorbed flux as a function of laser irradiance.

In the fast imaging studies of Apitz and Vogel (2005), the atmospheric pressure IR-laser ablation of water (70 ns Er:YAG laser pulse at 5.4 J/cm^2 fluence) clearly exhibited two phases: surface evaporation followed by a massive phase explosion. Initially, the rapid evaporation at the surface created a shock front that propagated away from the target. The advancing front was further accelerated by a delayed phase explosion. Quantitative analysis of the shock front position vs. time data in Fig. 9 of their publication is presented below to reveal this time delay, t_{pe}, and calculate the energy expended on surface evaporation, E_{se}, and on phase explosion, E_{pe}.

The similarity model, originally developed by Taylor for the description of nuclear explosions (Taylor, 1950), describes the time dependence of the shock front position, $R(t)$, as:

$$R(t) = S(\gamma)\rho_0^{-\frac{1}{5}}E^{\frac{1}{5}}t^{\frac{2}{5}}, \tag{1}$$

where $S(\gamma)$ is a weak function of the specific heat ratio, γ, ρ_0 is the background gas density and E is the energy of the explosion. Replotting the Apitz–Vogel data in the $t^{2/5}$ variable clearly demarcates the two phases (see Fig. 1).

Using the explosion analogy for the data in Fig. 1, one might presume that the two phases of the plume expansion correspond to the compounded effect of two consecutive "explosions." The first one corresponds to the abrupt onset of vigorous surface evaporation, whereas the second describes the phase explosion.

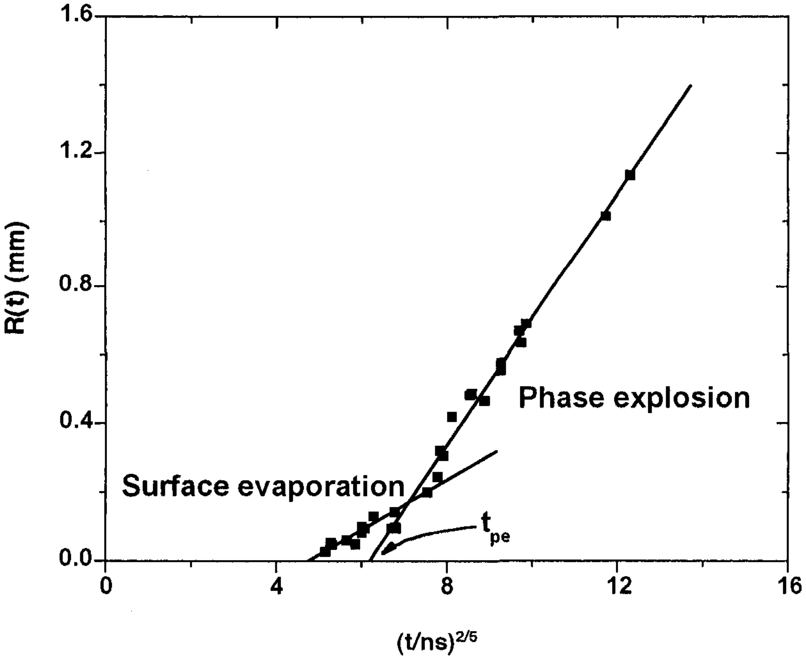

Figure 1. Shock front position as a function of time for Er:YAG laser ablation of water. Experimental data for 5.4 J/cm^2 fluence from Apitz and Vogel (2005) (■) replotted in $t^{2/5}$ variable. Solid lines indicate our linear fit using Eq. (1) for the surface evaporation and phase explosion.

Indeed, it is shown in Fig. 1 that Eq. (1) gives excellent fits to the data with a slope of 0.072 for surface evaporation, a slope of 0.186 for phase explosion, and with 0.89 and 0.99 regression coefficients, respectively.

From Eq. (1) and from the ratio of the slopes for the two phases of the expansion, q, one can determine the ratio of energies for the surface evaporation, E_{se}, and phase explosion, E_{pe}, processes:

$$q = \left(1 + \frac{E_{pe}}{E_{se}}\right)^{\frac{1}{5}}. \tag{2}$$

Because the laser pulse energy is primarily spent in the surface and volume processes, $E_l = E_{se} + E_{pe}$. From the total fluence and the slope ratio in Eq. (2), one can calculate the fluence fractions used in the two phases. From the slopes of the fitted curves in Fig. 1, $q = 2.57$ and the ratio of the two energies is, $E_{pe}/E_{se} = 111$. Thus, one can conclude that the overwhelming majority of the laser pulse energy is utilized in the volume process. In particular, only 0.05 J/cm^2 of the 5.4 J/cm^2 laser fluence drives the surface evaporation, whereas the remaining 5.35 J/cm^2 is used for the volume process. Extrapolating the second linear region back to $R(t_{pe}) = 0$ yields $t_{pe} = 94\ ns$, i.e., compared to the start of the laser pulse and even to the onset of the surface process the phase explosion is substantially delayed. This approach to extract the phase explosion delay and energy is valuable because there is no other method (experimental or theoretical) available to determine them.

Molecular dynamics simulations of the desorption process gave insight into the first 1 ns of the desorption process with exceptional detail. Early results revealed the fast disruption of hydrogen bond network in matrix solids due to laser heating, described the desorption of the analyte molecule through surface evaporation and followed the matrix guest energy transfer in MALDI (Bencsura and Vertes, 1995; Bencsura et al., 1997; Wu et al., 1998). Further investigations based on a simplified model potential that enabled the modeling of larger systems for a longer period of time found a transition from surface evaporation to phase explosion at elevated fluence values (Zhigilei et al., 1997). More detailed work indicated that longer laser pulses created thermal confinement conditions that resulted in a phase explosion, whereas shorter pulses induced stress confinement and photomechanical disintegration of the surface layers (Zhigilei and Garrison, 2000).

It is very likely that under typical MALDI conditions both surface evaporation and phase explosion contribute to the plume formation. Similar to the above analyzed water ablation scenario, the deposited laser energy initiates a rapid surface evaporation and, in case of nonlinear absorbers, creates a superheated subsurface layer. After a certain incubation period, t_{pe}, this metastable phase decomposes through phase explosion.

2.3 Ionization

Depending on the chemical nature of the matrix and the analyte, the ionization in MALDI can follow several paths. Often one can separate the formation of matrix ions (primary ions) in the condensed phase from analyte ionization (secondary ions) in the plume (Zenobi and Knochenmuss, 1998). Among the various mechanisms suggested for primary ion formation, perhaps the best supported is the one based on exciton pooling (Knochenmuss, 2002). This model is unique in the sense that it predicts several quantitative aspects of the MALDI process, such as the laser fluence threshold, the fluorescence yield for the most studied matrix, 2,5-DHB, and the ion yield. A refined version of the model (Knochenmuss, 2003) incorporates secondary ion formation through ion-molecule reactions in the plume and provides quantitative predictions for the ion suppression effects, for analyte ion yields and for the results of fast pump-probe experiments (Knochenmuss and Vertes, 2000).

In order to elucidate the relationship between matrix ionization and fragmentation, pumping rate studies were conducted using nanosecond and picosecond laser excitation (Chen and Vertes, 2003). Fig. 2 shows the dramatic difference in the fluence dependence of the molecular ion yields of 2,5-DHB for nitrogen laser (4 ns @ 337 nm) and for mode locked 3×ω Nd:YAG laser (22 ps @ 355 nm). This difference can be rationalized by the ladder climbing and ladder switching pathways outlined in the scheme below:

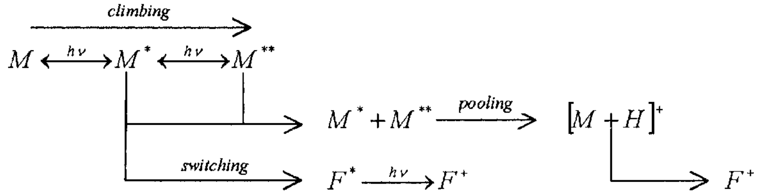

In the ladder climbing scheme, the singlet excited state, M*, of the matrix molecule, M, is further photoexcited to M**. The created mobile excitons combine to produce the protonated matrix species, $[M + H]^+$. Depending on its internal energy, this ion can thermalize or decompose into an F$^+$ fragment ion. In the ladder switching mode, the excited matrix molecules can directly break up into excited fragments, F*, and fragment ions, F$^+$.

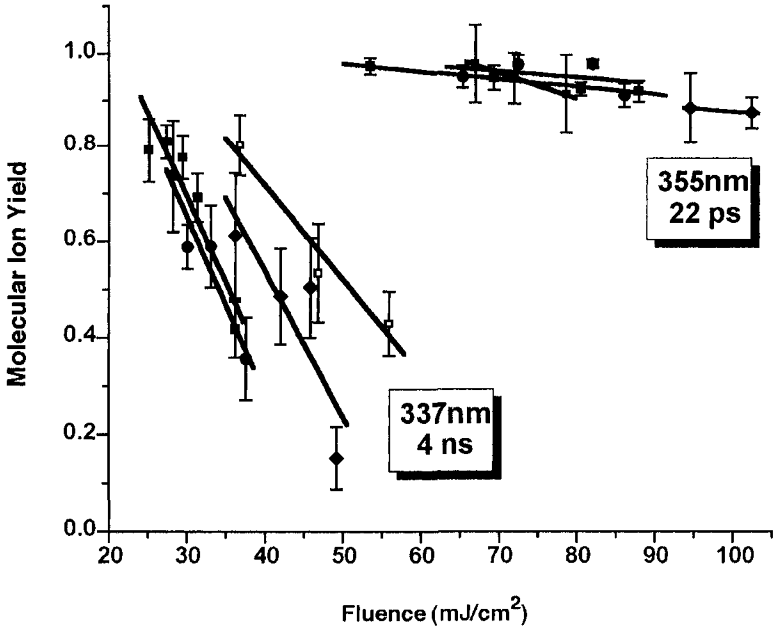

Figure 2. Molecular ion yields of 2,5-DHB pellets made with 100 MPa (■), 200 MPa (●) and 300 MPa (◆) pressure, and of dried droplet samples (□) measured with ns and with ps laser. Reprinted with permission from (Chen and Vertes, 2003). Copyright 2003 American Chemical Society.

Although both channels are active in MALDI, for ps excitation ladder climbing is dominant, whereas for ns laser pulses the relative contribution of ladder switching is larger. This mechanism is an extension of the photophysical model that can explain the large difference in molecular ion yields in Fig. 2. It also incorporates matrix fragmentation, a ubiquitous process in MALDI that clearly cannot be neglected.

The production of protonated analyte ions, $[A + H]^+$, and their fragments, AF^+, competes with adduct formation:

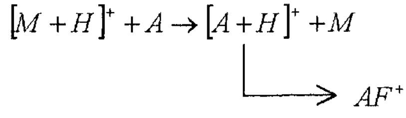
$$[M+H]^+ + A \rightarrow [A+H]^+ + M \rightarrow AF^+$$

$$F^+ + A \rightarrow [A+F]^+$$

The analyte ions are produced with significant internal energy resulting in metastable decay and fragmentation. These processes are further discussed in the following section.

2.4 Internal energy and fragmentation

In SLDI, there are two factors that determine the energy transfer and, correspondingly, the internal energy content of the analyte ions. The first one is associated with the desorption process (e.g., the phase transition of the matrix), whereas the second one is linked to the thermochemistry of ion formation.

In MALDI, the first component is controlled by the details of the phase transition (surface evaporation vs. phase explosion), the thermodynamic properties of the matrix (melting, boiling, spinodal decomposition and critical temperature, heats of melting and vaporization, and heat capacities in the different phases) and the transport properties (thermal conductivity) of the target (Luo, et al., 2002). Additional changes in the internal energy of ions can be induced by in-plume collisions with neutrals in the ion source (Gabelica, et al., 2004). This latter process occurs on a longer timescale and it is dependent on the characteristics of the ion source.

For protonated analytes, the energy transfer associated with the ionization primarily scales with the difference in gas phase basicities between matrix and analyte. A larger difference in gas phase basicities typically means high-

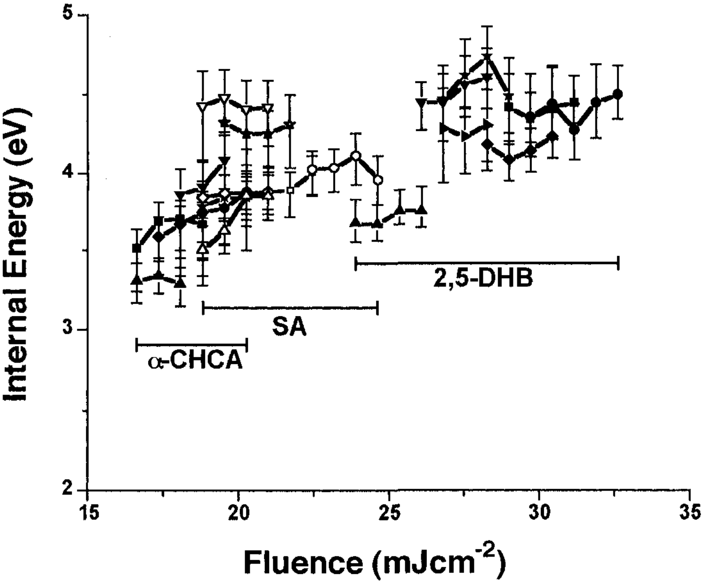

Figure 3. Fluence dependence of internal energies of preformed ions used as thermometer molecules in MALDI. Three different matrixes produced gas phase ions with internal energies increasing as α-CHCA < SA < 2,5-DHB. Data is from (Luo, et al., 2002). The horizontal bars indicate the utilized fluence ranges for the three matrixes. Different symbols correspond to the various thermometer ions. The symbols for SA matrix are hollow for better distinction.

er internal energy for the analyte ions (Stevenson, et al., 2000; Konn, et al., 2005).

Determining the internal energy transfer associated with the desorption process alone requires that the ionization step is eliminated. This was achieved by using the cations of benzyl-substituted benzylpyridinium salts as thermometer ions in MALDI (Luo et al., 2002). The ions of these salts are already preformed in the solid phase. Following their fragmentation in the MALDI process and measuring the survival yields for three matrixes (α-cyano-4-hydroxycinnamic acid (CHCA), 3,5-dimethoxy-4-hydroxycinnamic acid or sinapinic acid (SA) and 2,5-DHB) enabled the determination of the associated internal energies (see Fig. 3). The conversion from survival yields to internal energy was based on the Rice-Ramsperger-Kassel-Marcus (RRKM) theory of unimolecular decomposition.

The average internal energy values found for the different matrixes are 3.69±0.21 eV, 4.04±0.27 eV, and 4.30±0.29 eV for CHCA, SA, and 2,5-DHB, respectively. Compared to the previous qualitative assignment based on fragmentation patterns of small peptides (Stimson, et al., 1997), the CHCA<SA<2,5-DHB sequence of internal energies found for the thermometer ions shows the opposite trend.

This apparent contradiction is the consequence of the different processes involved. While the peptides in the earlier study undergo both desorption and protonation, and thus reflect the internal energy transfer associated with both, the thermometer ions only experience desorption. The opposite sequence of energy transfer from the same set of matrixes to neutral and ionic analytes highlights the comparable role desorption and ionization play in determining internal energy transfer. The internal energy content of the produced ions is the primary factor that determines their fragmentation and, in turn, our ability to infer structural information from SLDI mass spectra.

3. DESORPTION IONIZATION ON SILICON

The mass analysis of large molecules has been greatly facilitated by MALDI. For small molecules (<700 Da), however, the spectral interferences created by the ionic matrix species in this region present a key obstacle. Other limitations in MALDI stem from the solubility and cocrystallization requirements introduced by the sample preparation. Based on the SLDI approach, other methods are developed to alleviate these difficulties.

In the past fifteen years, the photoluminescent properties of porous silicon (pSi) fuelled a meticulous exploration of this low dimensional semiconductor. The application of pSi as an efficient matrix-free SLDI surface was discovered in 1999 (Wei, et al., 1999). This new approach was not only appealing because it did not produce interferences in the low mass region, but it also had the potential to be integrated into lab-on-a-chip devices.

The nanoporous structure of pSi is produced by photoelectrochemical etching of silicon wafers. For the typical n-type DIOS surfaces, the pore diameter distribution spans from nano- (<2 nm) to meso-scale (2-50 nm) and the porosity is 30 to 40% (Shen, et al., 2001). The pores can be several μm long; they are, on the average, perpendicular to the surface and are not interconnected. During the etching process, various surface species, such as hydrides, oxyhydrides, and oxides are formed (Cullis, et al., 1997).

Energy deposition in pSi exhibits some unique characteristics. The linear optical absorption coefficient of bulk silicon at the nitrogen laser wavelength of 337 nm is 10^6 cm^{-1} and between 300 and 972 K it is independent of temperature (Jellison and Modine, 1982). For pSi, at the same wavelength an effective absorption coefficient of up to 10^5 cm^{-1} can be observed (Kovalev, et al., 1996). The energy deposition, therefore, is very efficient in both systems. Due to limited dissipation through heat conduction in the thin pore walls (quasi-one-dimensional system), however, the temperature on the wall surfaces of pSi rises more rapidly and to a higher value than at the surface of bulk silicon.

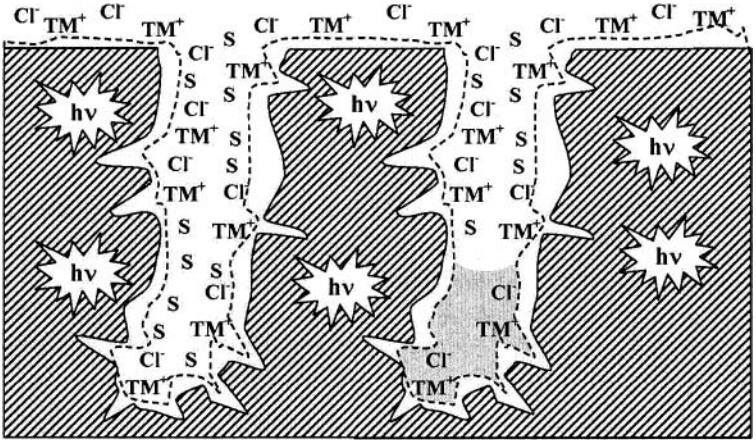

Figure 4. Adsorption of TM ions (TM^+ and Cl^-) and solvent molecules (S) in nanoporous silicon. Pore walls are sufficiently thin to induce thermal confinement and consequently high wall temperatures. **Left pore** only contains various adsorbates ("dry" desorption), whereas **right pore** shows trapped solvent (gray area) formed as a result of capillary condensation or retained due to inefficient pumping through nanopore ("wet" desorption). Reprinted with permission from (Luo, et al., 2005a). Copyright 2005 American Chemical Society.

This confinement of the deposited energy in the pore walls means that in pSi a particular surface temperature can be achieved at significantly lower laser fluence than in bulk silicon. Experimental results that are specific only to the desorption phase of the DIOS process are not yet available. Some conclusions on possible desorption mechanisms can be drawn from parametric studies and from ion yield measurements.

Investigations of the effect of laser wavelength, crystallographic orientation, preparation conditions, and other physical properties of the pSi (pore morphology, and thermal and optical properties) on ion generation were conducted to optimize the desorption conditions (Kruse, et al., 2001). There was no significant difference between DIOS mass spectra obtained at 266, 355 and 532 nm indicating much less sensitivity to wavelength than in MALDI. These experiments also proved that the porosity and wetting properties of the pSi substrate played a major role in determining DIOS ion yields but some of the other unique optical properties of the surface, i.e., photoluminescence, had no effect. Residual gases were identified as important factors in DIOS. When acetic acid or water vapor was introduced at a partial pressure of 2×10^{-6} Torr, it resulted in a 10 to 40-fold ion yield enhancement (Alimpiev, et al., 2001).

This observation highlights the importance of the trapped solvent and residual gas accumulated in the pores. Fig. 4 depicts two possible scenarios for the distribution of adsorbates in the pores. The left pore in Fig. 4 shows a "dry" environment, where the solvent and adsorbate molecules (in this case, thermometer cations and anions) compete for the adsorption sites. The right pore is "wet" due to the liquid solvent (gray area) either produced by capillary condensation or retained from sample preparation due to inefficient pumping through the nanopore.

The desorption of thermometer ions can proceed through either the dry or the wet pathway. As a result of energy deposition by the laser pulse, in the dry pores the rapid heating of the pore walls results in desorption of the adsorbates. In the confined space of the pores, a plume develops that undergoes one-dimensional expansion toward the mouth of the pore. During the expansion, the pressure is kept relatively high due to the confined space. In the wet pores the rapidly heated trapped solvent reaches the boiling and possibly the spinodal temperature. This gives rise to a high density solvent plume expanding with the released adsorbate.

Ionization of the adsorbed molecules can proceed through charged surface states (e.g., hydrides) or through ion-molecule reactions in the plume. As mentioned above, protons from the dissociation of water or acidic compounds can play a major role. The plume reactions, including

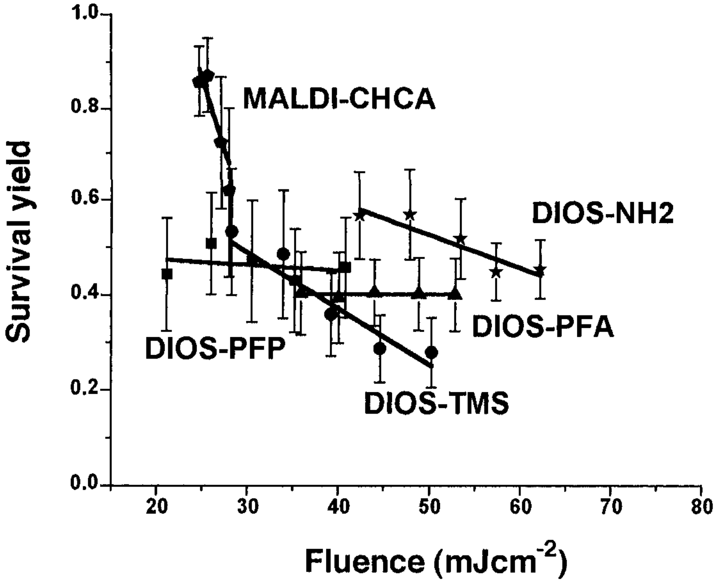

Figure 5. Comparison of survival yields for 3-methoxy-benzylpyridinium thermometer ions desorbed from four different DIOS surfaces with a nitrogen laser. Results for MALDI experiments using CHCA matrix are also included. Reprinted with permission from (Luo et al., 2005a). Copyright 2005 American Chemical Society.

protonation, are facilitated by the high density of the plume sustained by the confined space.

Using the survival yield of thermometer ions as a measure of internal energy, large differences between MALDI and DIOS were observed (Luo, et al., 2005a). Fig. 5 shows the fluence dependence of survival yields of guest ions for MALDI from CHCA matrix and for DIOS, from four derivatized surfaces. Trimethylsilyl- (TMS), amine- (NH2), perfluoroalkyl- (PFA), and perfluorophenyl (PFP) modification of the porous silicon was carried out to gauge the role of the hydrophilic character.

The survival yields in DIOS are uniformly lower than in MALDI with CHCA matrix. This is an indication that, perhaps as a result of plume confinement in the pores, DIOS imparts significantly more internal energy.

Indeed, comparing the dynamics of a quasi-one-dimensional and a three-dimensional expansion, the displacement of the shock front, *R(t)*, as described by the generalized form of Eq. (1) exhibits different kinetics (Sedov, 1993):

$$R(t) = \lambda_d \left(\frac{E}{\rho_1} \right)^{\frac{1}{2+d}} t^{\frac{2}{2+d}} . \tag{3}$$

In this expression, d is the dimension of the expansion, E is the deposited energy, ρ_l is the density of the environment, and λ_d is a dimension-dependent constant. Assuming similar conditions in MALDI and DIOS, the density of the background gas is expected to be higher in the latter due to the long and narrow pores. This results in a slower expansion. Furthermore, comparing the 1D and 3D expressions reveals a crossover in the position of the shock front at time

$$t_{co} = \left(\frac{\lambda_3}{\lambda_1} \right)^{\frac{15}{4}} \left(\frac{\rho_1}{E} \right)^{\frac{1}{2}} . \tag{4}$$

Initially, the radius of the 3D expansion exceeds the displacement in the 1D case, which, in turn, means lower density in the 3D expansion. Thus, t_{co} characterizes the time of confinement in a one-dimensional expansion. This confinement period also brings about faster energy transfer and higher reaction rates in the 1D case.

In Fig. 5, increasing the laser fluence within a narrow fluence range (~5 mJ/cm^2) leads to a sharp decline in the survival yields in MALDI, whereas, even in a wider fluence range (~20 mJ/cm^2), it produces very little change in DIOS. This has important implications for the stability of fragment ion production. While fragmentation in MALDI is strongly fluence dependent and fluctuates from laser shot to laser shot, the production of fragments shows much less variability in DIOS.

It is also apparent in Fig. 5, that the non-polar surface derivatized with PFP requires the lowest fluence, whereas the polar NH2 surface produces ions at significantly higher laser fluence. Considering the ionic nature of the adsorbed species, this behavior is expected. Doubling or even tripling the laser fluence, however, does not result in appreciable difference in the internal energy content of the desorbed ions. This unusual response is specific to DIOS and requires further investigation.

4. OTHER NANOSTRUCTURES

There is a large variety of other nanostructures that facilitate the SLDI of small to moderately sized biomolecules. Among the possible morphologies, quasi-one-dimensional systems such as nanopores in DIOS, nanowires, nanotubes, and nanogrooves stand out. They offer the lowest fluence threshold for ion production (nanowires) and the greatest versatility in terms of analytes. Nanoparticles, including quantum dots and nanoparticle films as well as ordered nanostructures such as nanocavities and silicon microcolumn arrays are being explored for SLDI applications. In the following subsections a few examples of these emerging nanostructures are discussed.

4.1 Nanowires

Semiconductor nanowires are of great interest for applications in nanoelectronics and as biological and chemical sensors. These quasi-one-dimensional systems can be produced by vapor-liquid-solid (VLS) methods using nanometer scale catalyst clusters (Yazawa, et al., 1992).

Gold clusters of 40 nm diameter as catalysts were deposited on silicon wafers and processed at 480°C in SiH_4 environment to produce the silicon nanowires shown in Fig. 6. To achieve the desired polarity, these nanowires were oxidized and silylated.

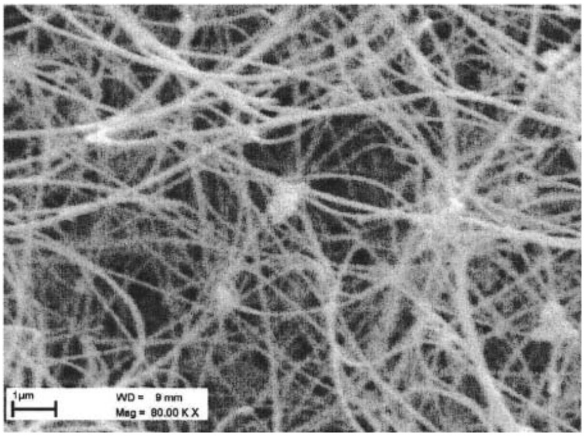

Figure 6. Scanning electron microscope (SEM) image of entangled silicon nanowires used in laser desorption experiments.

The ion yields of the species desorbed from these nanowires were investigated in SLDI mass spectrometry experiments (Go et al., 2005). A wide selection of small molecules and peptides were ionized with good efficiency. The nanowires exhibited significantly lower ionization fluence thresholds than DIOS surfaces or common MALDI matrixes. Correspondingly, the energy transfer during desorption from nanowires was limited. Fig. 7 shows the survival yields for 3-methoxy-benzylpyridinium thermometer cations in SLDI experiments. The fluence threshold for the nanowire surfaces was ~3 mJ/cm^2, whereas for DIOS it was ~21 mJ/cm^2. The lowest MALDI ion generation fluence was observed in CHCA matrix to be at ~25 mJ/cm^2.

The survival yields from PFP-derivatized nanowires were significantly higher than from PFP-DIOS surfaces and comparable to the ions desorbed from CHCA matrix in MALDI. The low fluence required for ion generation in combination with the high thermometer ion survival yields indicates that laser desorption from silicon nanowires is one of the gentlest SLDI methods we know.

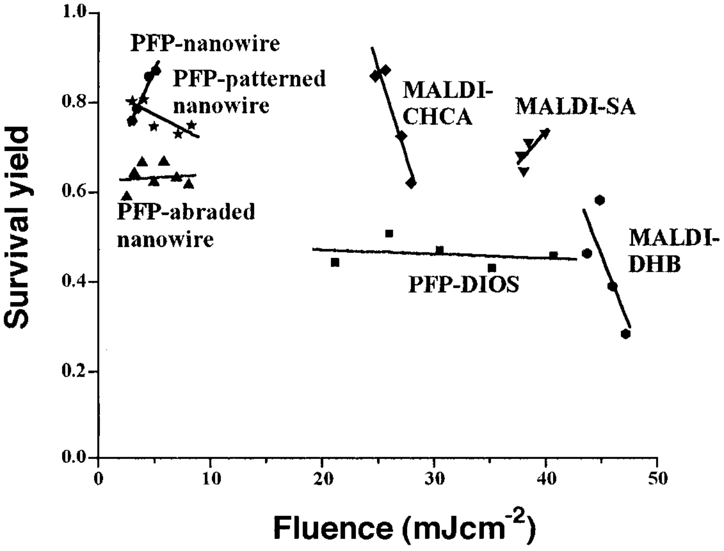

Figure 7. Comparison of survival yields of 3-methoxy-benzylpyridinium thermometer cations desorbed from native, patterned and abraded silicon nanowires, a perfluorophenyl-derivatized DIOS surface and from three different MALDI matrixes. Based on data in (Go et al., 2005). Copyright 2005 American Chemical Society.

4.2 Nanoparticles and nanoparticle films

Nanoparticles were first used in SLDI in 1988 (Tanaka, et al., 1988) but the efficiency of organic matrix materials displaced them for the following decade (Karas and Hillenkamp, 1988). In 1999, particle suspension matrixes were revisited (Schurenberg, et al., 1999) and it was noticed that the ion yields improved with decreasing particle size. Insulator, semiconductor, and metal particles were tested for their efficacy in facilitating ion production (Crecelius, et al., 2002; Turney, et al., 2004).

Recently, size selected gold nanoparticles were used in SLDI experiments (McLean et al., 2005). When the particle size was reduced from 10 nm to 2 nm, a significant improvement in peptide ion yield was observed. At the same time, the abundance of gold cluster ions diminished. This was interpreted as a consequence of quantum confinement in <3 nm gold particles. These results were obtained at relatively high laser pulse energy, 120 μJ/pulse, which raised the possibility that the experiments were carried out in a mixed ablation-desorption regime.

To further explore the laser fluence requirements, gold nanoparticle films were produced with the vertical colloidal deposition (VCD) technique (Diao, et al., 2003). First, 12 nm colloidal gold nanoparticles were produced by solution phase Na_2S reduction of $HAuCl_4$. Then, evaporation-driven VCD was used to produce the nanoparticle films with uniform particle distribution. When these films were used as SLDI substrates, compared to earlier nanoparticle studies (McLean et al., 2005) ion yield measurements on small peptides indicated a significantly reduced threshold at 3 to 4 μJ/pulse (Chen et al., 2005; Luo et al., 2005b). The produced mass spectra were completely free of gold cluster ions. This served as an indication that on the nanoparticle film surfaces ablation did not play a role in ion generation.

The nanoparticle films offer additional advantages over individual particles. Unlike the particles that tend to aggregate and coalesce, the VCD surfaces are very stable and require 30 to 40 times reduced laser pulse energy for ion generation.

4.3 Silicon microcolumn arrays

Silicon microcolumn arrays are very robust structures that spontaneously develop under a wide range of conditions when a silicon wafer is exposed to repeated laser pulses at a certain fluence level. Initially, cone array formation was observed when aluminum oxide (Al_2O_3) target in vacuum was exposed to a few hundred 6 ns laser pulses at 266 nm wavelength and 0.5 J/cm^2 fluence (Rothenberg and Kelly, 1984). In 1998, silicon microcolumn arrays were produced by femtosecond laser processing (Her, et al., 1998). Low resistivity silicon wafers in 500 Torr SF_6 environment were exposed to 500 pulses of 800 nm laser radiation with 100 fs pulse length at 1 J/cm^2 fluence.

At these fluences periodic surface structures seem to develop irrespective of the environmental pressure (from vacuum to atmospheric pressure), laser wavelength (from near IR to near UV), and laser pulse length (from 100 fs to 6 ns). In a pulse length study, however, it was noted that 100 fs pulses gave a column separation of 10 µm and increasing the pulse length to 10 ps resulted in column arrays with 5 µm periodicity (Her et al., 2000). At 250 ps pulse length no columns were observed.

To explore the ps pulse length range, 22 ps pulses from a mode-locked 3×ω Nd:YAG laser (355 nm) were used to process low resistivity silicon wafers (Chen and Vertes, 2005; Chen, et al., 2005). Microcolumn arrays were produced under a wide range of environmental conditions, including ambient air, 10 Torr SF_6 and liquid water (see Fig. 8). The formation of the microcolumn structures required 1000 to 1200 laser pulses with 0.4–1.0 J/cm^2 fluence.

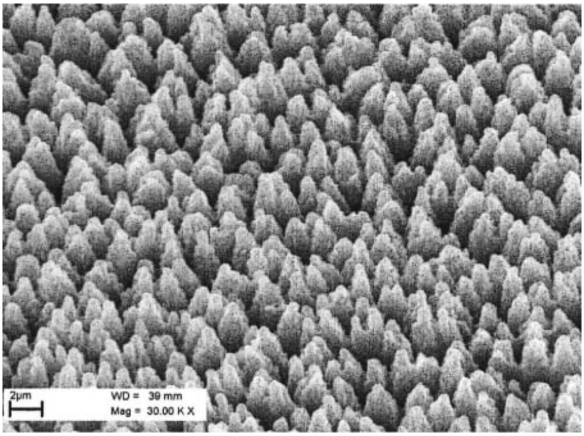

Figure 8. Tilted (45°) SEM view of silicon microcolumn array produced in water with 1000 pulses of a mode locked 3×ω Nd:YAG laser at 355 nm wavelength. The 22 ps pulses delivered 0.4 J/cm^2 fluence.

These results indicate that near UV laser pulses of tens of ps in duration can successfully create silicon microcolumn arrays. Of the tested preparation methods, the aqueous environment produced the columns with the sharpest tips, i.e., with less than 500 nm in diameter.

Silicon microcolumn arrays were used in their native state as desorption surfaces for SLDI of small peptides, including, angiotensin I, substance P, insulin, and their mixtures. In the spectra, up to m/z ~6000 predominantly protonated ions were observed. The submicron tip diameter microcolumn arrays produced in water demonstrated the highest ion yields with a threshold fluence of ~30 mJ/cm^2 that was comparable to values observed in MALDI. Fig. 9 shows the SLDI spectrum of substance P desorbed from a silicon microcolumn array substrate produced in 10-Torr SF_6 gas environment.

Although other silicon nanostructures, such as nanopores and nanowires, are also used to produce peptide ions in SLDI experiments, the silicon microcolumn surfaces are significantly simpler to produce and can be more readily integrated into microchemical chips. Due to the uniform light absorption characteristics of the surface from near UV to mid-IR, it is expected that a wide variety of lasers can be used for SLDI experiments.

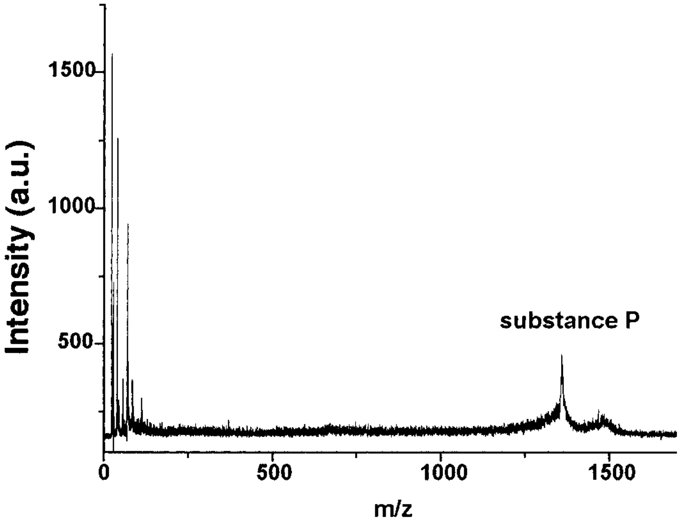

Figure 9. Mass spectrum of substance P with SLDI at a laser fluence of ~75 mJ/cm^2. Silicon microcolumn array substrate was produced in 10 Torr SF$_6$ gas environment using 1200 pulses of 1 J/cm^2.

It is unclear if the SLDI experiments reported here for silicon microcolumn arrays utilize the specific properties of the array. The effect of the periodicity, the column length and the incidence angle of the laser radiation has not yet been studied. Exploring the effect of these parameters is necessary to improve our understanding of how these ordered systems facilitate SLDI.

5. OUTLOOK

In the past one and a half decades, the analysis of biomolecules has greatly benefited from the improved mass accuracy of MALDI mass spectrometry. Based on the achievements, MALDI has become a mainstream method. Further refinements of the method are primarily expected in particular applications and in its novel combinations with separation techniques.

For the analysis of small to medium size molecules, matrix-less desorption surfaces, such as DIOS and other nanostructures are being explored. These emerging methods exhibit broad applicability in the analysis of small biomolecules and pharmaceuticals.

The interaction of laser light with nanostructures also presents new challenges in our understanding how coherent electromagnetic radiation interacts with systems that exhibit quantum confinement, nanoscopic liquid confinement and confined reactions. The dimensions of nanostructures can be commensurate to the wavelength of the radiation and thus give rise to near field effects in desorption and ionization. Based on the improved understanding of these phenomena, new "designer" surfaces can be envisioned that are specifically created to enhance SLDI.

Other potential developments include the integration of SLDI nanostructures into chip-based analytical methods. Combining the separation and the spectroscopic steps in a single device promises improved efficiency and higher throughput in biomedical analysis.

6. ACKNOWLEDGMENTS

Funding for some of the research described in this chapter was provided by grants from the U.S. Department of Energy (DE-FG02-01ER15129), the W. M. Keck Foundation (041904) and the George Washington University Research Enhancement Fund (GWU-REF). Support from the Department of Energy does not constitute an endorsement of the views expressed in the article. The author is grateful for the Academy Award Fellowship of the Royal Flemish Academy of Belgium for Science and the Arts. Discussions with A. Vogel were helpful in clarifying the experimental details of the water ablation data.

7. REFERENCES

Alimpiev, S., Nikiforov, S., Karavanskii, V., Minton, T., and Sunner, J., 2001, On the mechanism of laser-induced desorption–ionization of organic compounds from etched silicon and carbon surfaces, *J. Chem. Phys.* **115**(4):1891–1901.

Allwood, D. A., Dreyfus, R. W., Perera, I. K., and Dyer, P. E., 1996, UV optical absorption of matrices used for matrix-assisted laser desorption/ionization, *Rapid Commun. Mass Spectrom.* **10**(13):1575–1578.

Allwood, D., Dreyfus, R., Perera, I., and Dyer, P., 1997, Optical absorption of matrix compounds for laser-induced desorption and ionization (MALDI), *Appl. Surf. Sci.* **109/110**:154–157.

Allwood, D., and Dyer, P., 2000, Quantitative fluorescence measurements performed on typical matrix molecules in matrix-assisted laser desorption/ionisation, *Chem. Phys.* **261**(3):457–467.

Apitz, I., and Vogel, A., 2005, Material ejection in nanosecond Er:YAG laser ablation of water, liver, and skin, *Appl. Phys. A* **81**(2):329–338.

Bencsura, A., Navale, V., Sadeghi, M., and Vertes, A., 1997, Matrix-Guest Energy Transfer in Matrix-Assisted Laser Desorption, *Rapid Commun. Mass Spectrom.* **11**(6):679–682.

Bencsura, A., and Vertes, A., 1995, Dynamics of hydrogen bonding and energy transfer in matrix-assisted laser desorption, *Chem. Phys. Letters* **247**(1-2):142–148.

Beuhler, R. J., Flanigan, E., Greene, L. J., and Friedman, L., 1974, Proton transfer mass spectrometry of peptides. A rapid heating technique for underivatized peptides containing arginine, *J. Am. Chem. Soc.* **96**(12):3990–3999.

Chen, Y., Luo, G., Diao, J., Chornoguz, O., Reeves, M., and Vertes, A., 2005, Laser desorption/ionization from nanostructured surfaces: nanowires, nanoparticle films and silicon microcolumn arrays, *J. Phys.: Conf. Ser.* in press.

Chen, Y., and Vertes, A., 2003, Pumping rate and surface morphology dependence of ionization processes in matrix-assisted laser desorption ionization, *J. Phys. Chem. A* **107**(46):9754–9761.

Chen, Y., and Vertes, A., 2005, Black silicon as matrix-free laser desorption ionization substrate, *Abstracts of Papers, 230th ACS National Meeting*, Washington, DC, United States, Aug. 28-Sept. 1, 2005, **2005**(111):ANYL.

Crecelius, A., Clench, M. R., Richards, D. S., and Parr, V., 2002, Thin-layer chromatography–matrix-assisted laser desorption ionisation–time-of-flight mass spectrometry using particle suspension matrices, *J. Chromatogr. A* **958**(1-2):249–260.

Cullis, A. G., Canham, L. T., and Calcott, P. D. J., 1997, The structural and luminescence properties of porous silicon, *J. Appl. Phys.* **82**(3):909–965.

Diao, J. J., Qiu, F. S., Chen, G. D., and Reeves, M. E., 2003, Surface vertical deposition for gold nanoparticle film, *J. Phys. D Appl. Phys.* **36**:L25–L27.

Dreisewerd, K., 2003, The desorption process in MALDI, *Chem. Rev.* **103**(2):395–425.

Finkel, N. H., Prevo, B. G., Velev, O. D., and He, L., 2005, Ordered silicon nanocavity arrays in surface-assisted desorption/ionization mass spectrometry, *Anal. Chem.* **77**(4):1088–1095.

Gabelica, V., Schulz, E., and Karas, M., 2004, Internal energy build-up in matrix-assisted laser desorption/ionization, *J. Mass Spectrom.* **39**(6):579–593.

Go, E. P., Apon, J. V., Luo, G., Saghatelian, A., Daniels, R. H., Sahi, V., Dubrow, R., Cravatt, B. F., Vertes, A., and Siuzdak, G., 2005, Desorption/ionization on silicon nanowires, *Anal. Chem.* **77**(6):1641–1646.

Her, T.-H., Finlay, R. J., Wu, C., Deliwala, S., and Mazur, E., 1998, Microstructuring of silicon with femtosecond laser pulses, *Appl. Phys. Lett.* **73**(12):1673–1675.

Her, T.-H., Finlay, R. J., Wu, C., and Mazur, E., 2000, Femtosecond laser-induced formation of spikes on silicon, *Appl. Phys. A* **70**(4):383–385.

Jellison, Jr., G. E., and Modine, F. A., 1982, Optical absorption of silicon between 1.6 and 4.7 eV at elevated temperatures, *Appl. Phys. Lett.* **41**(2):180–182.

Juhasz, P., Vestal, M. L., and Martin, S. A., 1997, On the initial velocity of ions generated by matrix-assisted laser desorption ionization and its effect on the calibration of delayed extraction time-of-flight mass spectra, *J. Am. Soc. Mass Spectrom.* **8**(3):209–217.

Karas, M., and Hillenkamp, F., 1988, Laser desorption ionization of proteins with molecular masses exceeding 10 000 Daltons, *Anal. Chem.* **60**(20):2299–2301.

Knochenmuss, R., 2002, A quantitative model of ultraviolet matrix-assisted laser desorption/ionization, *J. Mass Spectrom.* **37**(8):867–877.

Knochenmuss, R., 2003, A quantitative model of ultraviolet matrix-assisted laser desorption/ionization including analyte ion generation., *Anal. Chem.* **75**(10):2199–2207.

Knochenmuss, R., and Vertes, A., 2000, Time-delayed 2-pulse studies of MALDI matrix ionization mechanisms, *J. Phys. Chem. B* **104**(23):5406–5410.

Konn, D. O., Murrell, J., Despeyroux, D., and Gaskell, S.J., 2005, Comparison of the effects of ionization mechanism, analyte concentration, and ion "cool-times" on the internal energies of peptide ions produced by electrospray and atmospheric pressure matrix-assisted laser desorption ionization, *J. Am. Soc. Mass Spectrom.* 16(5): 743–751.

Kovalev, D., Polisski, G., Ben-Chorin, M., Diener, J., and Koch, F., 1996, The temperature dependence of the absorption coefficient of porous silicon, *J. Appl. Phys.* **80**(10):5978–5983.

Kruse, R.A., Li, X., Bohn, P. W., and Sweedler, J. V., 2001 Experimental factors controlling analyte ion generation in laser desorption/ionization mass spectrometry on porous silicon, *Anal. Chem.* **73**(15):3639–3645.

Luo, G., Chen, Y., Siuzdak, G., and Vertes, A., 2005a, Surface modification and laser pulse length effects on internal energy transfer in DIOS, *J. Phys. Chem. B* **109** (51): 24450-24456

Luo, G., Diao, J., Chornoguz, O., Reeves, M., and Vertes, A., 2005b, Laser desorption/ionization mass spectrometry from nanoparticle films, *Abstracts of Papers, 230th ACS National Meeting*, Washington, DC, United States, Aug. 28-Sept. 1, 2005, **2005**(109):ANYL.

Luo, G. H., Marginean, I., and Vertes, A., 2002, Internal energy of ions generated by matrix-assisted laser desorption/ionization, *Anal. Chem.* **74**(24):6185–6190.

McLean, J. A., Stumpo, K. A., and Russell, D. H., 2005, Size-selected (2-10 nm) gold nanoparticles for matrix assisted laser desorption ionization of peptides, *J. Am. Chem. Soc.* **127**(15):5304–5305.

Menzel, C., Dreisewerd, K., Berkenkamp, S. and Hillenkamp, F., 2001, Mechanisms of energy deposition in infrared matrix-assisted laser desorption/ionization mass spectrometry, *Int. J. Mass Spectrom.* **207**(1/2): 73–96.

Okuno, S., Arakawa, R., Okamoto, K., Matsui, Y., Seki, S., Kozawa, T., Tagawa, S., and Wada, Y., 2005, Requirements for laser-induced desorption/ionization on submicrometer structures, *Anal. Chem.* **77**(16):5364–5369.

Posthumus, M. A., Kistemaker P. G., Meuzelaar H. L. C., and Ten Noever de Brauw M. C., 1978, Laser desorption–mass spectrometry of polar nonvolatile bio-organic molecules, *Anal. Chem.* **50**(7):985–991.

Rothenberg, J. E., and Kelly, R., 1984, Laser sputtering. Part II. The mechanism of the sputtering of Al_2O_3, *Nucl. Instrum. Meth. Phys. Res. B* **229**(2-3):291–300.

Sadeghi, M., and Vertes, A., 1998, Crystallite size dependence of volatilization in matrix-assisted laser desorption ionization, *Appl. Surf. Sci.* **127/129**:226–234.

Schurenberg, M., Dreisewerd, K., and Hillenkamp, F., 1999, Laser desorption/ionization mass spectrometry of peptides and proteins with particle suspension matrixes, *Anal. Chem.*, **71**(1):221–229.

Sedov, L. I., 1993, *Similarity and Dimensional Methods in Mechanics*, 10-th ed., CRC Press, Boca Raton.

Shen, Z. X., Thomas, J. J., Averbuj, C., Broo, K. M., Engelhard, M., Crowell, J. E., Finn, M. G., and Siuzdak, G., 2001, Porous silicon as a versatile platform for laser desorption/ionization mass spectrometry, *Anal. Chem.* **73**(3):612–619

Stevenson, E., Breuker, K., and Zenobi, R., 2000 Internal energies of analyte ions generated from different matrix-assisted laser desorption/ionization matrices, *J. Mass Spectrom.* **35**(8):1035–1041.

Stimson, E., Truong, O., Richter, W. J., Waterfield, M. D., and Burlingame, A. L., 1997, Enhancement of charge remote fragmentation in protonated peptides by high-energy CID MALDI-TOF-MS using "cold" matrices, *Int. J. Mass Spectrom. Ion Processes* **169/170**:231–240.

Tanaka, K., Waki, H., Ido, Y., Akita, S., Yoshida, Y., and Yoshida, T., 1988, Protein and polymer analyses up to m/z 100 000 by laser ionization time-of-flight mass spectrometry, *Rapid Commun. Mass Spectrom.* **2**(8):151–153.

Taylor, G., 1950, The Formation of a Blast Wave by a Very Intense Explosion. I. Theoretical Discussion, *Proc. Roy. Soc. London A* **201**(1065):159–174.

Turney, K., Drake, T. J., Smith, J. E., Tan W., and Harrison, W. W., 2004, Functionalized nanoparticles for liquid atmospheric pressure matrix-assisted laser desorption/ionization peptide analysis, *Rapid Commun. Mass Spectrom.* **18**(20):2367–2374.

Vertes, A., Irinyi, G., and Gijbels, R., 1993, Hydrodynamic model of matrix assisted laser desorption mass spectrometry," *Anal. Chem.* **65**(17):2389–2393.

Wei, J., Buriak, J. M., and Siuzdak, G., 1999, Desorption-ionization mass spectrometry on porous silicon, *Nature* **399**(6733): 243–246.

Wu, X., Sadeghi, M., and Vertes, A., 1998, Molecular dynamics of matrix-assisted laser desorption of leucine enkephalin guest molecules from nicotinic acid host crystal, *J. Phys. Chem. B* **102**(24):4770–4778.

Xu, S., Li, Y., Zou, H., Qiu, J., Guo, Z., and Guo, B., 2003, Carbon nanotubes as assisted matrix for laser desorption/ionization time-of-flight mass spectrometry, *Anal. Chem.* **75**(22):6191–6195.

Yazawa, M., Koguchi, M., Muto, A., Ozawa, M., and Hiruma, K., 1992, Effect of one monolayer of surface gold atoms on the epitaxial growth of InAs nanowhiskers, *Appl. Phys. Lett.* **61**(17):2051–2053.

Zenobi, R., and Knochenmuss, R., 1998, Ion formation in MALDI mass spectrometry, *Mass Spec. Rev.* **17**(5):337–366.

Zhigilei, L. V., and Garrison, B. J., 2000, Microscopic mechanisms of laser ablation of organic solids in the thermal and stress confinement irradiation regimes, *J. Appl. Phys.* **88**(3):1281–1298.

Zhigilei, L. V., Kodali, P. B. S., and Garrison, B. J., 1997, Molecular dynamics model for laser ablation and desorption of organic solids, *J. Phys. Chem. B* **101**(11):2028–2037.